#### **OPEN ACCESS**



# Constraining the Properties of the Multicomponent Local Interstellar Medium: MHD-kinetic Modeling Validated by Voyager and New Horizons Data

Federico Fraternale 10, Nikolai V. Pogorelov 1,20, and Ratan K. Bera 10.

1 Center for Space Plasma and Aeronomic Research, University of Alabama in Huntsville, Huntsville, AL 35805, USA; federico.fraternale@uah.edu

2 Department of Space Science, University of Alabama in Huntsville, Huntsville, AL 35805, USA

Received 2024 June 21; revised 2024 September 19; accepted 2024 September 20; published 2024 October 7

#### **Abstract**

We introduce the first solar-cycle simulations from our 3D, global MHD-plasma/kinetic-neutrals model, where both hydrogen and helium atoms are treated kinetically, while electrons and helium ions are described as individual fluids. Using Voyager/PWS observations of electron density up to 160 au from the Sun for validation of several different global models, we conclude that the current estimates for the proton density in the local interstellar medium (LISM) need a revision. Our findings indicate that the commonly accepted value of 0.054 cm<sup>-3</sup> may need to be increased to values exceeding 0.07 cm<sup>-3</sup>. We also show how different assumptions regarding the proton velocity distribution function in the outer heliosheath may affect the global solution. A new feature revealed by our simulations is that the helium ion flow may be significantly compressed and heated in the heliotail at heliocentric distances exceeding ~400 au. Additionally, we identify a Kelvin–Helmholtz instability at the boundary of the slow and fast solar wind in the inner heliosheath, which acts as a driver of turbulence in the heliotail. These results are crucial for inferring the properties of the LISM and of the global heliosphere structure.

Unified Astronomy Thesaurus concepts: Interstellar medium (847); Heliosphere (711); Heliopause (707); Interstellar plasma (851); Astrosphere interstellar medium interactions (106); Charge exchange ionization (2056) Materials only available in the online version of record: animations

#### 1. Introduction

The heliosphere, which exists because of the interaction between the solar wind (SW) and the local interstellar medium (LISM), is a natural laboratory allowing studies of the plasma processes occurring on a range of scales and parameters impossible to replicate in a terrestrial setting. Only a handful of missions currently provide data from the outer heliosphere, i.e., Voyager 1 and 2 (V1, V2), Interstellar Boundary Explorer (IBEX), and New Horizons (NH). The Interstellar Mapping and Acceleration Probe (IMAP) mission (D. J. McComas et al. 2018), scheduled for launch in 2025, will provide higher-resolution neutral atom measurements, which may further reveal the properties of the heliospheric boundaries.

Hereinafter we will use the term very local interstellar medium (VLISM) to denote the fraction of the LISM perturbed in various ways by the presence of the heliosphere (G. P. Zank 2015; F. Fraternale & N. V. Pogorelov 2021). Models suggest that this region extends over a thousand au in the upwind direction and potentially spans 10 times that distance downwind. The presence of a bow shock (BS) and the properties of the outer heliosheath (OHS) region are contingent on the details of the global SW-LISM interaction. Interstellar neutral (ISN) atoms can reach 1 au and have been used as a tool to infer the properties of the unperturbed LISM (e.g., R. Lallement et al. 2005). However, because of the selective filtration of neutral atoms in the OHS and their time-dependent ionization in the SW regions, the velocity distribution functions (VDFs) of ISN atoms are strongly modified. ISN atoms experience charge exchange in the inner heliosheath (IHS) and

Original content from this work may be used under the terms of the Creative Commons Attribution 4.0 licence. Any further distribution of this work must maintain attribution to the author(s) and the title of the work, journal citation and DOI.

outer heliosheath (OHS), producing secondary neutrals and nonthermal pickup ions (PUIs). PUIs of IHS and OHS origin give birth to so-called energetic neutral atoms (ENAs). Both the ISN and ENA fluxes, observed at 1 au by IBEX, enable remote studies of the global heliosphere (e.g., D. J. McComas et al. 2009; J. Heerikhuisen et al. 2010; D. B. Reisenfeld et al. 2021).

Several questions about the properties of the unperturbed LISM remain unanswered. Recent studies, supported by PUI measurements made by NH, have focused on reevaluating the commonly accepted estimates of the LISM parameters. (see, e.g., P. Swaczyna et al. 2020, 2023, 2024; F. Fraternale et al. 2023). These challenging tasks require extensive theoretical analyses and global modeling efforts. Due to their complicated, anisotropic VDFs, neutral atoms should be modeled kinetically.

ISN helium is of particular importance because of its smaller charge-exchange cross sections as compared to neutral hydrogen and its relatively high abundance. However, the distributions of He atoms, even of the primary ones, which experience no charge exchange until they reach the IBEX detectors, deviate from a Maxwellian distribution (e.g., B. E. Wood et al. 2019; F. Fraternale et al. 2021). There is a possibility that He ENAs, not measured by IBEX but likely to be detected by IMAP in the future, may provide important information on the structure of the heliosphere (e.g., S. Grzedzielski et al. 2013).

In this study, for the first time, we address the challenging task of performing time-dependent, fully 3D, MHD-plasma/kinetic-neutrals simulations with both H and He atoms and validate results with electron density data from V1. Our goal is to provide a more accurate picture of the time-dependent SW-LISM interaction and to improve the estimates of the properties of the LISM that is close to the heliosphere but remains unperturbed by it.

**Table 1**Boundary Conditions and the List of Performed Simulations

Parameter	Units	Value	Description
		Outer Boundary	v: LISM
$n_{\rm p,LISM}$	$\mathrm{cm}^{-3}$	0.054/0.068/0.075	LISM proton density
$n_{\mathrm{He}^+,\mathrm{LISM}}$	$\mathrm{cm}^{-3}$	0.00898	LISM He <sup>+</sup> density (M. Bzowski et al. 2019)
$n_{ m H,LISM}$	$\mathrm{cm}^{-3}$	0.195	LISM H density (P. Swaczyna et al. 2020)
$n_{\mathrm{He,LISM}}$	$\mathrm{cm}^{-3}$	0.0153	LISM He density (G. Gloeckler et al. 2004)
$V_{ m LISM}$	${\rm km~s}^{-1}$	-25.4	LISM bulk flow speed (D. J. McComas et al. 2015)
$(\lambda_{V, \text{LISM}}, \beta_{V, \text{LISM}})$	deg	(255.°7, 5.°1)	LISM flow direction (Ecliptic J2000) (D. J. McComas et al. 2015)
$T_{ m LISM}$	K	7,500	LISM temperature (all species) (D. J. McComas et al. 2015)
$B_{LISM}$	nT	0.293	ISMF strength (D. J. McComas et al. 2015)
$(\lambda_{B, LISM}, \beta_{B, LISM})$	deg	(227°.28, 34°.62)	ISMF direction (ecliptic J2000) (E. J. Zirnstein et al. 2016)
		Inner Boundary at 1 au: Sola	ar Cycle Simulation <sup>a</sup>
$B_r$	nT	3.75	Radial HMF component; dipolar magnetic field
$V_f$	${\rm km~s}^{-1}$	750	Fast SW speed (all species)
$V_s$	${\rm km~s}^{-1}$	415	Slow SW speed (all species)
$T_{f,p}; T_{f,He^{2+}}$	K	$250,000; 10^6$	Fast SW temperature
$T_{s,p,}; T_{s,He^{2+}}$	K	80,000; 400,000	Slow SW temperature
$n_{f,p}; n_{f,He^{2+}}$	$\mathrm{cm}^{-3}$	2.1; 0.0875	Fast SW number density
$n_{s,p}; n_{s,He^{2+}}$	$\mathrm{cm}^{-3}$	7.2; 0.2	Slow SW number density
		Simulation	ns
		-3; Maxwellian plasma; LS05 cross	s sections <sup>b</sup>
B steady-state; kinetic H, I C steady-state; kinetic H, I			

D steady-state; kinetic H, He;  $n_{\rm p,LISM} = 0.075~{\rm cm}^{-3}$ ;  $n_{\rm He^+,LISM} = 0.01~{\rm cm}^{-3}$ ; Maxwellian plasma

#### Notes.

We build on the most recent extension of the Multi-Scale Fluid-Kinetic Simulation Suite (MS-FLUKSS), which includes electrons as a separate, charge-neutralizing fluid (F. Fraternale et al. 2023). Global, time-dependent simulations, involving only the kinetically described H atoms, were performed earlier by V. V. Izmodenov et al. (2005), J. Heerikhuisen et al. (2013), E. J. Zirnstein et al. (2015), and V. V. Izmodenov & D. B. Alexashov (2020). However, the technique utilized by the former authors is only applicable for finding time-periodic solutions. In this Letter, we add time-dependent, kinetic He atoms and present a solar cycle simulation with high resolution in the entire SW-LISM interaction region, including the heliotail. We present an updated version of the model that includes alpha particles in the SW and discuss the implications of adding helium to the global model.

Our model is introduced in Section 2 and described in detail in Appendix A. Results are presented in Section 3. The details about the challenges associated with time-dependent kinetic neutral H and He atoms are given in Appendix B.

#### 2. Physical Model and Boundary Conditions

Our physical model includes an MHD description of plasma (detailed in Appendix A) and a kinetic description for neutral H

and He atoms (Appendix B). The most recent version is described in F. Fraternale et al. (2024). We also introduce a modified description of helium ions by solving the equations for two distinct species in two different environments:  $\mathrm{He}^{2+}$  ions (alpha particles) in the SW, and  $\mathrm{He}^+$  ions in the LISM. In fact, the density of  $\mathrm{He}^{2+}$  ions in the SW at 1 au is higher by approximately a factor of  $10^3$  than that of  $\mathrm{He}^+$  ions. The  $\mathrm{He}^{2+}$  ions in the SW carry a significant fraction of dynamic pressure (8%-20% of the proton pressure), which ultimately contributes to the pressure balance at the heliopause (HP).

In a time-dependent scenario, an iterative procedure, traditionally used in steady-state calculations, cannot be applied. We have implemented a strategy that enables us to find a self-consistent solution that describes both spatial and temporal inhomogeneities in the neutral atom distributions throughout the heliosphere (see Appendix B).

The boundary conditions (BCs) used in the simulations presented here are summarized in Table 1. The solar cycle model is the same as was used by N. V. Pogorelov et al. (2009), where the latitudinal extent of the boundary between the fast and slow SW changes periodically from 28° to 90° from the ecliptic plane over 11 yr, whereas the tilt angle between the Sun's rotation and magnetic axes varies from 8° to 90°. In this

E steady-state; kinetic H, He;  $n_{\rm p,LISM} = 0.068~{\rm cm}^{-3}$ ; kappa SW + kappa OHS protons ( $\kappa = 1.63$ )<sup>c</sup>

F steady-state; kinetic H, He;  $n_{\rm p,LISM} = 0.068~{\rm cm}^{-3}$ ; kappa SW protons;  $\alpha_{\rm BV} = 20^{\circ}$ 

G nominal solar cycle; multifluid H; separate PUIs;  $n_{\rm p,LISM} = 0.054~{\rm cm}^{-3}$ ; Maxwellian plasma, no He ions and atoms

H nominal solar cycle; kinetic H, He;  $n_{\rm p,LISM} = 0.068~{\rm cm}^{-3}$ ; Maxwellian plasma

<sup>&</sup>lt;sup>a</sup> For the steady-state simulations A-F, the inner BCs are given in F. Fraternale et al. (2024).

 $<sup>^{\</sup>rm b}$  Simulations  $^{\rm B-H}$  use updated cross sections as described in Appendix A.

<sup>&</sup>lt;sup>c</sup> Here the OHS protons are kappa distributed at the HP out to 150 au, then smoothly transitioning to a Maxwellian distribution up to heliocentric distance of 350 au, beyond which the VDF becomes fully Maxwellian.

model, the properties of fast and slow SW at 1 au are constant over time, being translated analytically to 10 au as in F. Fraternale et al. (2023). These properties, including the  $He^{2+}/H^{+}$ density and temperature ratios, are chosen to be consistent with the Ulysses and ACE data and slightly adjusted to achieve the same ram pressure in the fast and slow SW. Our model assumes all species to be comoving. This assumption implies that the velocity shear between different species, on the MHD scale, tends to vanish owing to wave-particle interaction and turbulence and also to Coulomb collisions, particularly in the LISM. As far as He<sup>2+</sup> ions are concerned, Ulysses data have shown that the He<sup>2+</sup>-H<sup>+</sup> velocity shear decreases steadily with radial distance, becoming  $\sim 10 \, \mathrm{km \, s^{-1}}$  at 5 au (M. Neugebauer et al. 1996; P. Mostafavi et al. 2022). The velocity shear close to the Sun plays a role in the heating of He<sup>2+</sup> ions. We take into account the nonadiabatic temperature profile of He<sup>2+</sup> ions in the inner heliosphere, assuming a polytropic index of 1.4 (only at R < 10 au).

The bottom section of Table 1 lists the simulations performed in this study. Simulation A corresponds to the best models presented in F. Fraternale et al. (2023; S3 therein), where, for the source term calculations, the plasma is assumed to be Maxwellian everywhere and the LS05 cross sections are employed. The proton density in the LISM  $(n_{p,LISM})$  is equal to  $0.054 \,\mathrm{cm}^{-3}$ . Simulations B and D use higher densities of 0.068 and 0.075 cm<sup>-3</sup>, respectively. Simulation C uses the same BCs as in case B, but protons are kappa distributed in the SW. Simulation E represents a scenario where protons are kappa distributed both in the SW and in the OHS. While this scenario might not be realistic, it serves as a proof of concept to demonstrate the importance of the VLISM ion VDF in global solutions. Simulation F demonstrates the effects of a decreased angle between the LISM magnetic field and velocity vectors. Simulation G refers to multifluid solar cycle calculations without helium and with PUIs treated separately. Finally, case H presents our new time-dependent simulation of the solar cycle.

#### 3. Results and Discussion

Recent V1/PWS data reveal the existence of a radial gradient of the electron density,  $n_{\rm e}$ , that extends from the HP to at least 160 au from the Sun (W. S. Kurth 2024). Electron density values are obtained from the frequency measurements corresponding to both electron plasma oscillation (epo) events and those associated with a narrowband emission line at the plasma frequency (fpe) (D. A. Gurnett et al. 2021; S. Ocker et al. 2021). These distributions are shown in Figure 1 with the results from our steady-state and time-dependent modeling. While the radial gradient is evident in the data, it is affected by the outward-propagating shocks and/or compression waves that "climb up" the background positive gradient. This behavior has been accurately reproduced by the previous time-dependent and data-driven global models (T. K. Kim et al. 2017; N. V. Pogorelov et al. 2021). It should be noted that the observed density remains as high as  $\sim 0.15 \, \mathrm{cm}^{-3}$  since the last pressure front crossing in 2020.5 (from 150 to 162 au). Note also that the data points shown in Figure 1 represent a temporal time series in which the radial distance refers to the spacecraft position at different times, which is the reason for the shocks to appear reversed.

The Voyager/PWS data constitute a robust constraint on the global models. As seen from Figure 1, models with helium underestimate the electron density observed by V1 in the

VLISM for the consensus parameters of the unperturbed LISM (F. Fraternale et al. 2023). To our knowledge, this issue has not been addressed in the literature. Moreover, model validations based on the electron data have never been performed.

A commonly adopted value for the LISM proton density,  $n_{\rm p.LISM} = 0.054 \, {\rm cm}^{-3}$ , was obtained by M. Bzowski et al. (2019) by fitting ISN He observations from IBEX-Lo with the aid of time-independent global simulations with the LISM H and plasma nucleon densities of 0.154 and 0.089 cm<sup>-3</sup>, respectively. Such values typically ensure a good agreement between the observed HP position in V1 data (121.6 au) and global simulations (see Figure 5 of N. V. Pogorelov et al. 2017b), when it is assumed that  $n_{\rm p,LISM} = 0.089 \, {\rm cm}^{-3}$  and  ${\rm He}^+$  ions are absent, and hence  $n_p \equiv n_e$ . However, when using the same LISM plasma nucleon density but including He<sup>+</sup> ions  $(n_{\text{He}^+,\text{LISM}} = 0.009 \text{ cm}^{-3})$ , thereby using the proton density of  $n_{\rm p,LISM} = 0.054 \, {\rm cm}^{-3}$ , the V1/PWS data cannot be reproduced. This is shown with the red curve in Figure 1, representing the result from simulation A (S3 in F. Fraternale et al. 2023). It shows that  $n_{\rm e}$  is underestimated by approximately 36%. It is unlikely that this may be explained with time dependence alone. Even data-driven simulations that reproduce the V1 magnetic field observations in the OHS assumed  $n_{\rm p,LISM} = 0.089$  to compensate for the absence of helium (T. K. Kim et al. 2017).

To address this discrepancy between the simulations and data, several factors should be considered, e.g., modifications to  $n_{\rm p,LISM}$ ,  $n_{\rm He^+,LISM}$ , neutral atom densities, and interstellar magnetic field (ISMF),  $\boldsymbol{B}_{\rm LISM}$ .

We have previously shown that varying the LISM H density from 0.15 to 0.22 cm<sup>-3</sup> does not result in significant changes to the maximum value of  $n_e$  (R. K. Bera et al. 2023; F. Fraternale et al. 2023), which remains around 0.1 cm<sup>-3</sup> in those simulations.

It is known that the ISMF magnitude and orientation have significant implications for the modeled properties of plasma and neutral atom properties in the OHS (e.g., G. P. Zank et al. 2013). So far, F. Fraternale et al. (2023) have used the best-fit ISMF parameters derived by E. J. Zirnstein et al. (2016) based on the IBEX ribbon analysis, also used by T. K. Kim et al. (2017). Our unperturbed LISM flow is only marginally superfast magnetosonic, and we have demonstrated how the presence of helium affects the transition between superfast and subfast flow regimes. Previous simulations show that the peak value of  $n_e$  in the V1 direction is (i) inversely correlated with the strength of the ISMF and (ii) inversely correlated with the angle between the magnetic field and velocity vectors ( $\alpha_{\rm BV} = \cos^{-1}|\hat{\pmb{B}}_{\rm LISM}\cdot\hat{\pmb{V}}_{\rm LISM}|$ ; see, e.g., Figure 2 in N. V. Pogorelov et al. 2017b). Furthermore, to maintain the HP at the same standoff distance, the LISM plasma density must increase as the ISMF strength and  $\alpha_{\rm BV}$  decrease. These use a fixed orientation of the B-V plane, defined by the velocity and magnetic field vectors in the unperturbed LISM.

However, the ISMF parameters remain a subject of debate. V. V. Izmodenov & D. B. Alexashov (2020) found the best fit of their time-dependent global model to Voyager data using conditions  $\alpha_{\rm BV}=60^{\circ}$  and  $B_{\rm LISM}=0.38$  nT. They also obtained a second solution with  $\alpha_{\rm BV}=20^{\circ}$  and  $B_{\rm LISM}=0.44$  nT. Recent works by M. Kornbleuth et al. (2024) and E. Powell et al. (2024) address this topic based on modeling ENA observations from the heliotail and Ly $\alpha$  absorption data, respectively, using their steady-state model. The former study suggests that the angle  $\alpha_{\rm BV}$  may be as small as 10°, while  $\alpha_{\rm BV}=40^{\circ}$  provides the best-fit parameters in the latter study. Both studies suggest

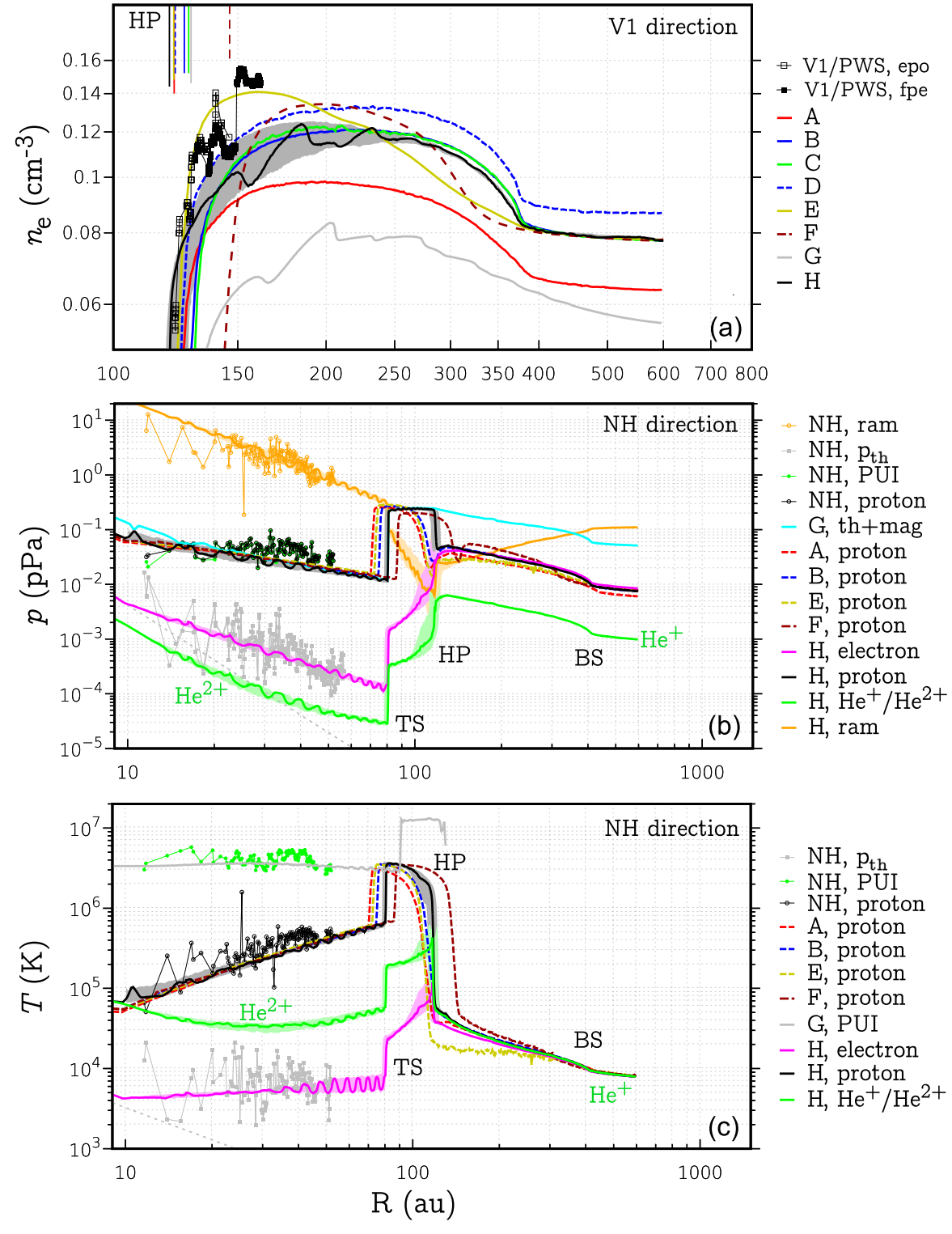


Figure 1. (a) Comparison of the electron density observed by V1/PWS in the OHS with several global simulations labeled from A to H as in Table 1. (b) Pressures along the radial trajectory corresponding to the mean direction of NH trajectory (ecliptic latitude of  $2^{\circ}$  and longitude of  $285^{\circ}$ ) are compared with the NH data (D. J. McComas et al. 2022) for thermal protons ( $p_{th}$ ; gray points), PUIs (green), and the proton mixture (black). (c) Temperature distributions in simulation H; an arbitrary time instant is visualized, and the variability over the last three simulated solar cycles is shown with shaded areas.

that the ISMF strength is around 0.3 nT. Previous Ly $\alpha$  modeling efforts by G. P. Zank et al. (2013) also found a better agreement for a field strength of 0.3 nT,  $\alpha_{\rm BV} \sim 47^{\circ}$ , and an LISM nucleon density of 0.09 cm<sup>-3</sup>. We conclude that increasing either  $B_{\rm LISM}$  or  $\alpha_{\rm BV}$  compared to our baseline parameters would not help toward the issue of fixing the

discrepancy with V1/PWS electron density data. We use the new simulation F to explore the possibility of a small angle,  $\alpha_{\rm BV}=20^{\circ}$ , while keeping  $B_{\rm LISM}=0.293\,{\rm nT}$  and the other parameters the same as in case C.

Leaving aside the considerations regarding  $n_{H,LISM}$  and the ISMF, we now focus on the ion densities. It is evident that

increasing only  $n_{\rm He^+}$  by a factor of  $\sim 2$  would introduce an excessive ram pressure, due to the mass ratio. While we do not exclude the possibility that the accepted values of  $n_{\rm He^+}$  may also need a revision, our investigation focuses on the effects of increasing  $n_{\rm p,LISM}$  up to  $\sim 0.075~{\rm cm}^{-3}$ . The degrees of ionization in our new simulations are  $\chi_{\rm H}=n_{\rm H^+}/(n_{\rm H}+n_{\rm H^+})\in[0.259,\,0.278]$  and  $\chi_{\rm He}=n_{\rm He^+}/(n_{\rm He}+n_{\rm He^+})\in[0.370,\,0.395]$ , and the He<sup>+</sup> to hydrogen density ratio is  $(n_{\rm He^+}/n_{\rm H})_{\rm LISM}\in[0.046,\,0.052]$ . These quantities remain compatible with those published by J. D. Slavin & P. C. Frisch (2008) and later revisited by M. Bzowski et al. (2019).

Including a realistic density of He<sup>2+</sup> ions in the SW is necessary and sufficient to keep the HP at a distance similar to that in our previous simulations compatible with Voyager observations. As shown in Figure 1(a), the underestimation of  $n_{\rm e}$  is reduced in the new simulations compared to simulation A, although the values still align with the lower bound of V1/PWS observations, indicating the need for further improvements. Importantly, the comparison with NH data remains satisfactory in all these simulations, as shown in panels (b) and (c). We note that the most recent NH data at  $\sim$ 50 au align well with our results, while the observed proton (PUI-dominated) pressure and temperature are comparably higher at distances from  $\sim$ 32 to  $\sim$ 45 au. We are not overly concerned by this discrepancy, likely due to a time-dependent effect related to changes in the dynamic pressure at 1 au, not included in the model. This and other features have been reasonably reproduced in data-driven simulations with MS-FLUKSS (T. Kim et al. 2018). Until more realistic BCs are tested with our new model, we cannot draw conclusions about potential systematic discrepancies or determine whether additional heating of PUIs is required in the model. The new simulations also show an increase of over 20% in proton temperature in the IHS compared to case A.

Using a kappa distribution for protons only in the SW (case C) does not lead to significant changes in the heliosheath width. This is due to the energy dependence of the charge-exchange cross section, as explained, e.g., by A. M. DeStefano & J. Heerikhuisen (2020).

However, remarkable changes are observed in the distributions of plasma when kappa distributions are assumed for protons in both the SW and OHS (case E). One can see a notable increase in the radial gradient of electron density in the VLISM near the HP and a decrease in the heliocentric distance toward the peak of  $n_e$ . The same occurs with the peak in H density in the hydrogen wall, due to the increased average mean free path for charge exchange in this scenario. Moreover, the temperature of protons in the OHS adjacent to the HP decreases from ~40,000 K in cases A-D to approximately 25,000 K in case E. These values are all consistent with V2 thermal proton observations (J. D. Richardson et al. 2019). It is possible that protons in the OHS have a core, mainly consisting of the secondary protons born when primary ISN atoms chargeexchange with the decelerated ions and a tail of nonthermal (pickup) protons born when the neutralized SW atoms experience charge exchange in the VLISM (e.g., J. Heerikhuisen et al. 2016). However, the exact shape of the ion VDF in the OHS is unknown. Therefore, proposed simulation E serves only as a proof of concept, likely illustrating an extreme case. It highlights the importance of refining our understanding of the VLISM ion VDFs.

Solution F, as expected, results in a stronger BS. The maximum electron density in the OHS becomes higher compared to the simulations with  $\alpha_{\rm BV} = 40^{\circ}$ . Still, the peak value is slightly below V1 observation, which confirms our conclusions that the LISM proton density should be higher than 0.054 cm<sup>-3</sup>. However, there are issues with this simulation because the HP standoff distance becomes 149 au and the IHS is wider compared to the other simulations, which is not supported by Voyager observations. Notably, the same occurs in the V. V. Izmodenov & D. B. Alexashov (2020) solution with  $\alpha_{\rm BV} \sim 20^{\circ}$ , where the HP in the V1 direction exceeds 160 au. One cannot rule out the possibility of fixing this issue, e.g., by further increasing the LISM plasma density (as was done in Model 1 of G. P. Zank et al. 2013 and N. V. Pogorelov et al. 2017b) or the LISM flow speed. We note that such adjustments further support the conclusions of this Letter, but we are not addressing them in detail here.

The results from case H, the first of the solar cycle simulations in the presence of kinetically treated H and He atoms, are shown in Figures 2, 3, and 4. Figure 2 shows the distributions of number density, pressure, and temperature of protons (the mixture of thermal and PUIs), helium ions, and electrons in the B-V plane. The effects of relatively cold electrons in the SW at heliocentric distances less than ~350 au in this time-dependent simulation are similar to those obtained in our prior steady solutions (F. Fraternale et al. 2023). However, the unstable columns of collimated plasma, which originate in the polar regions, now disappear because of the dominant solar cycle dynamics. This is a well-known phenomenon described previously by N. V. Pogorelov et al. (2015). It is of interest to look at Figure 2, which shows the properties of He<sup>2+</sup> ions in the heliotail beyond  $\sim 400$  au. The He<sup>2+</sup> pressure and temperature are found to increase substantially with distance tailward. A similar behavior is observed for electrons, their temperature exceeding  $2.5 \times 10^{5}$  K beyond  $\sim 400$  au from the Sun. Such accumulation of charged particles and their heating seem to be related, via the conservation laws, to a slowdown of the plasma flow in the tail, which is associated with the cooling of protons due to charge exchange and compression of the tail by the ISMF. As a consequence, protons cool down with distance even faster than in the solutions without helium ions. Charge exchange of He<sup>2+</sup> ions with He atoms and Coulomb collisions both contribute to their cooling in the distant tail (see Figure 4(c)) but are not very efficient. Thus, an additional compression does not result in a significant deviation from adiabatic behavior. These results will need further verification by adding charge exchange of He2+ ions with H and He atoms that will generate He<sup>+</sup> ions. This is expected to have important implications for the production of helium ENAs and to possibly shed more light on the properties of the heliotail.

Figure 3 illustrates the heliospheric structures through visualizations of the current density (J) and flow vorticity ( $\Omega$ ) magnitudes, nucleon density, and azimuthal component of magnetic field. The heliotail cross sections at 400 and 900 au from the Sun at an arbitrary time instant show that the heliotail remains unsplit, which confirms the previous results of N. V. Pogorelov et al. (2017b). The dipolar nature of the HMF is of great importance for the heliotail topology. We emphasize that the two "lobes" visible in panels (c) and (d) correspond to confined regions of hotter plasma originating from the fast SW, which alternate with colder, denser SW regions and have HMF polarity opposite to that in the

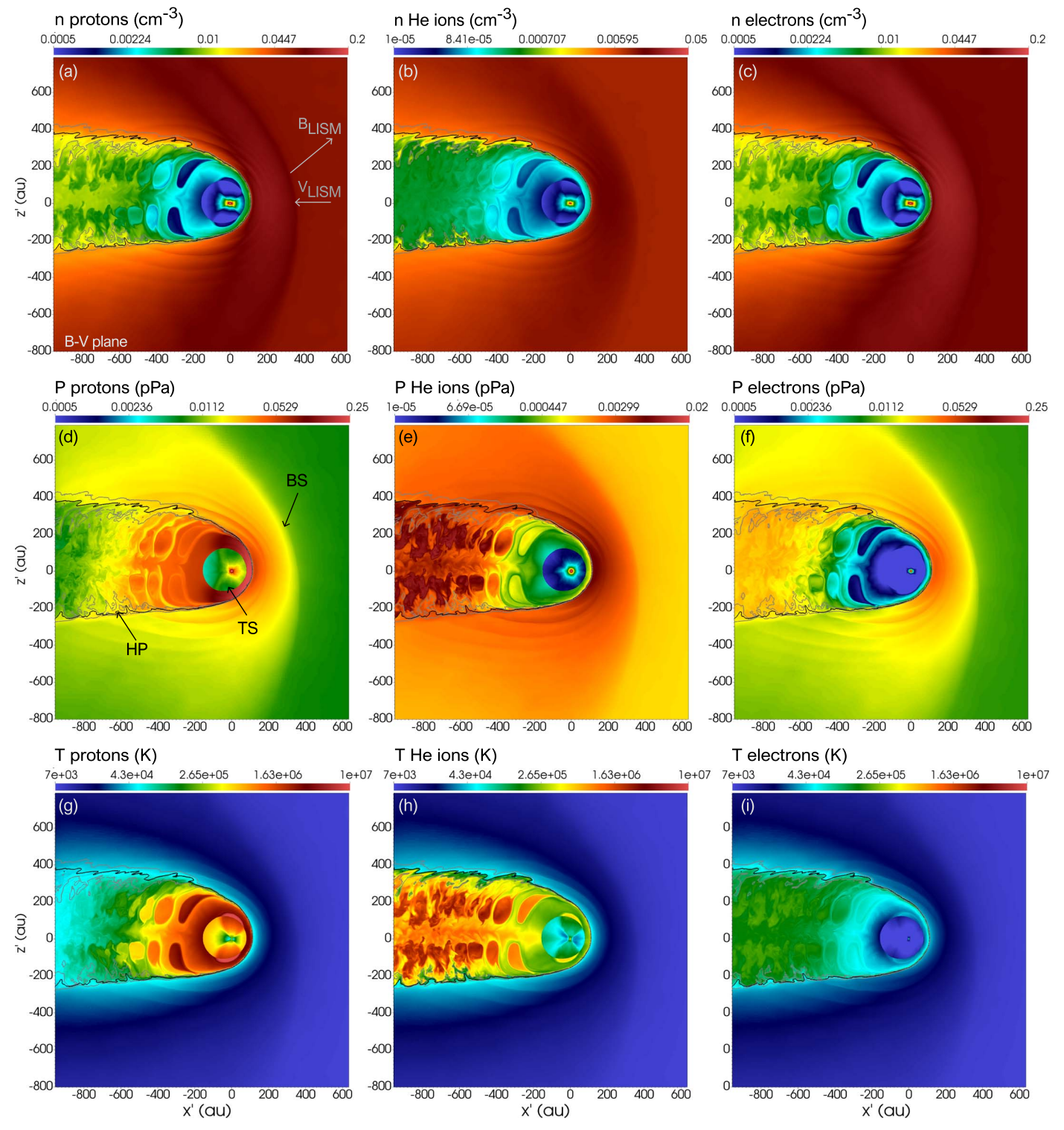


Figure 2. Plasma distributions in the B-V plane from simulation H. From top to bottom we show the number density, pressure, and temperature. From left to right the quantities are shown for protons (including the core and PUIs), He ions, and electrons. The black contours show the HP position (defined by the LS  $\psi = 0$ ). Additionally, two gray contours of  $\psi = \pm 0.98$  offer qualitative insights about the extent of mixing and numerical diffusion of the SW and LISM at the HP.

preceding or subsequent hot region. They should not be confused with the long columns of collimated plasma that undergo instability in unipolar solutions (see discussions and Figure 10 in F. Fraternale et al. 2023). This type of instability does not occur in the solar cycle simulations, even if the HMF is kept unipolar and does not reverse polarity. This numerical

experiment was presented by N. V. Pogorelov et al. (2017a) and recently replicated by F. Fraternale et al. (2024).

Despite the SW-LISM mixing at the HP, caused by the large-scale Kelvin-Helmholtz instability (KHI), and partially due to unavoidable numerical diffusion, the HP can still be identified by strong shears in magnetic field and velocity. This

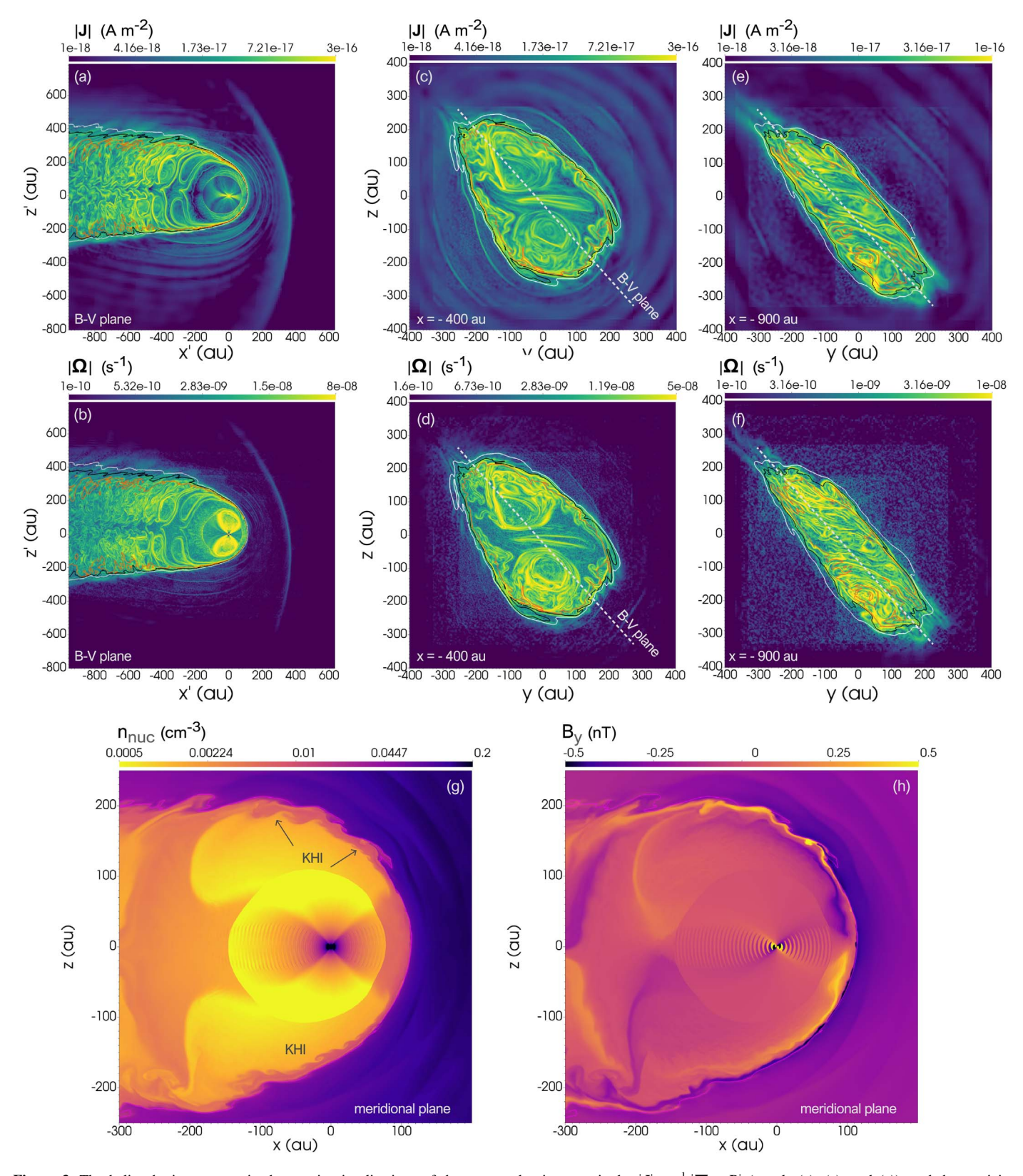
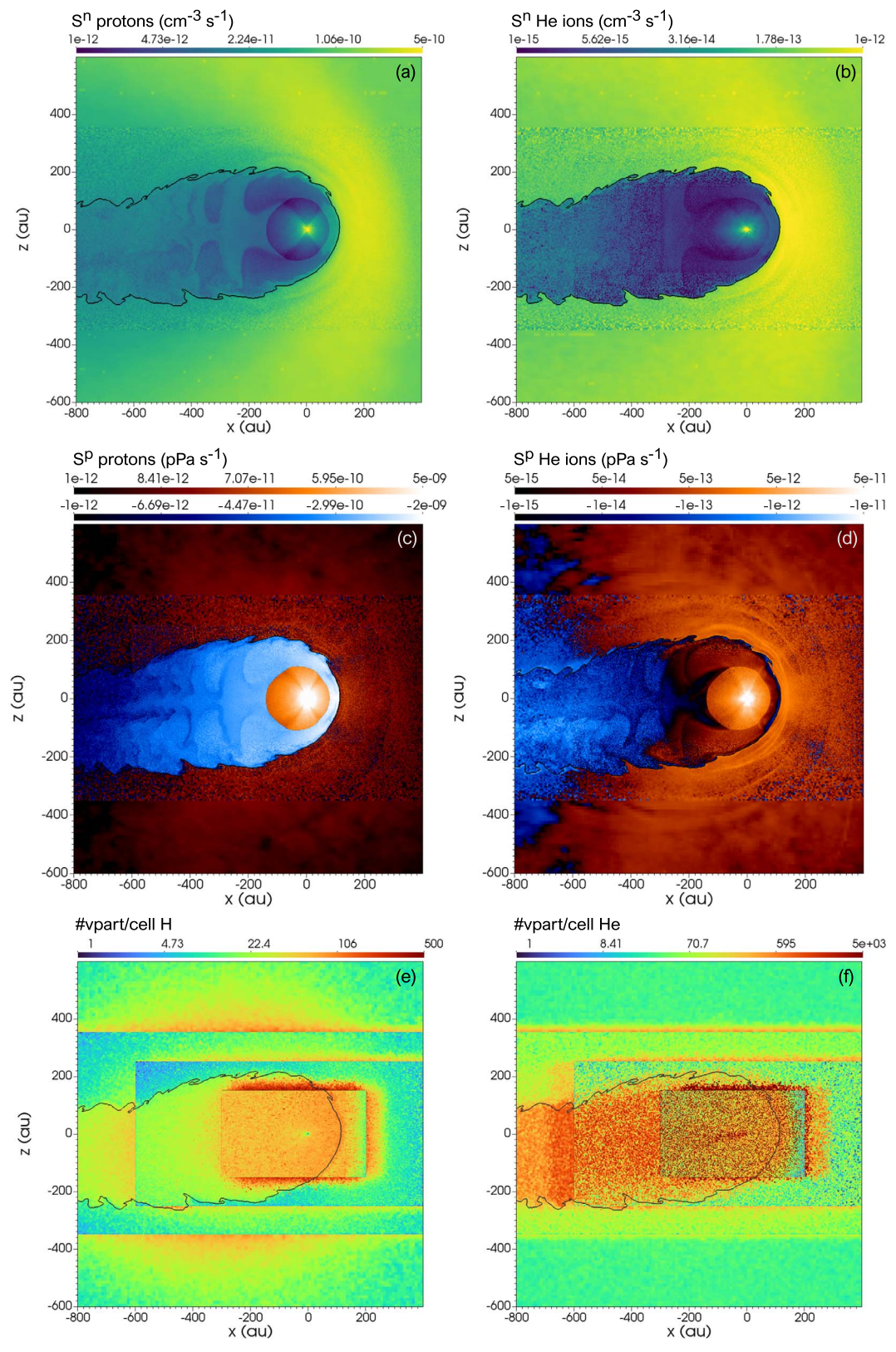


Figure 3. The heliospheric structure is shown via visualizations of the current density magnitude,  $|J| = \mu_0^{-1} |\nabla \times B|$  (panels (a), (c), and (e)), and the vorticity magnitude,  $|\Omega| = |\nabla \times u|$  (panels (b), (d), and (f)). Panels (a) and (b) show the quantities in the B-V plane, while panels (c) and (d) and panels (e) and (f) show cross sections of the heliotail made at 400 and 900 au from the Sun, respectively. The contour lines for the HP are as in Figure 2. The bottom panels show the nucleon density and the azimuthal magnetic field component in the meridional (x-z) plane. An animation of panel (g) is provided online, showing the time evolution over 50 yr (duration 16 s).

(An animation of this figure is available in the online article.)



**Figure 4.** Kinetic source terms. The top panels show the rate of production of new ions by charge exchange, per unit volume. The middle panels show the thermal pressure source term due to charge exchange of H and He atoms. Two different color maps are used for the positive and negative values. The animated version of panels (c) and (d) combined, provided online, shows the time evolution over 50 yr (duration 16 s). The bottom panels show the number of virtual macroparticles per cell of the kinetic grid where the source terms are gathered. The left and right panels show the same quantities for hydrogen and helium atoms, respectively. (An animation of this figure is available in the online article.)

figure also demonstrates that the level-set (LS) contour  $\psi = 0$  (red curves) aligns with the contours of J and  $\Omega$ .

In the upwind part of the IHS, the heliosphere largely preserves the main features found by N. V. Pogorelov et al. (2017b) in solutions without helium. Additionally, a new feature has been identified, i.e., a KHI occurring in the IHS at high latitudes and in the polar regions (see Figure 3(g)). This instability reveals itself at the interface of the fast and slow (and denser) winds spreading over the inner side of the HP at all phases of the solar cycle. It is triggered during the declining phases of the cycle, when the fast wind occupies progressively lower latitudes in the IHS, and reaches maximum amplitudes near solar maxima. Charge exchange and related momentum transfer are enhanced in the slow wind layer (see Figure 4), which likely contributes to enhancements in the velocity shear. This instability contributes to driving turbulence in the tail.

Figure 4 shows the production of new (pickup) ions per unit time and volume, the thermal pressure sources due to ionization of hydrogen and helium ions, and the number of virtual (split) particles per cell. It demonstrates that an accurate description of the kinetic source terms can be achieved by running the kinetic stage for only 0.2 yr (see Appendix B). Notably, while the variability of the source terms is primarily due to the changes in plasma (see, e.g., the effect of shocks propagating in the VLISM, the role of the fast/slow SW boundary, etc.), the simulation also captures the effects associated with time-dependent ENAs. This is particularly evident from the animation of Figures 4(c) and (d) available online.

### 4. Summary

Using kinetic models that take into account the presence of helium ions and atoms is of crucial importance for modeling the SW–LISM interaction. This study demonstrates the importance of using Voyager/PWS electron density observations in the OHS to validate numerical models. By comparing different simulation results, we suggest that the proton density in the unperturbed LISM should exceed  $\sim 0.07 \, \mathrm{cm}^{-3}$ .

We have developed a time-dependent version of the kinetic model for H and He atoms and discussed its implementation and associated challenges. This model is crucial, as it makes it possible to derive time-dependent VDFs of neutral atoms, including the energetic component (ENAs). We have presented the first solar cycle simulation based on this model, which produces a comet-like heliosphere with a turbulent tail. Notably, we identify a KHI at the boundary between fast and slow SW in the IHS, which contributes to driving turbulence in the heliotail region.

Our simulations also suggest that a significant increase in temperature and pressure of helium ions may occur in the heliotail beyond approximately 400 au. While these results require additional confirmation by future models incorporating both He<sup>2+</sup> and He<sup>+</sup> ions in the SW and additional ionization and recombination processes, they may have significant implications for the interpretation of future IMAP observations of He ENAs that may be used as a tool for inferring the global heliospheric structure.

# Acknowledgments

This work is supported by NASA grants 80NSSC24K0267 and 80NSSC22K0524. It was also supported by the IBEX

mission (PI D. J. McComas) as part of NASA's Explorer Program (80NSSC18K0237). We are thankful to W. S. Kurth for providing the recent V1/PWS data. We acknowledge the Texas Advanced Computing Center (TACC) at the University of Texas at Austin for providing HPC resources on Frontera supported by NSF award CISE-OAC-2031611. Supercomputer time allocations were also provided by NASA High-End Computing Program awards SMD-17-1537 and SMD-23-67004198 and by NSF ACCESS project MCA07S033. We are grateful to the International Space Science Institute (ISSI) in Bern, for its support through ISSI International Team project No. 23-574, "Shocks, Waves, Turbulence, and Suprathermal Electrons in the Very Local Interstellar Medium," and No. 21-541, "Distribution of Interstellar Neutral Hydrogen in the Sun's Neighborhood."

## Appendix A Plasma Description (MHD)

Our plasma description is based on the solution of a system of MHD conservation laws for plasma and separate auxiliary equations for the density and pressure of helium ions and electrons, as detailed by F. Fraternale et al. (2024). The multifluid model G treats PUIs as a separate fluid but does not include equations for helium ions (R. K. Bera et al. 2023). We use the terms  $S_s^{\rho,m,E,p}$  to indicate the source terms in the mass, momentum, energy, and pressure equations. These source terms are due to charge exchange for each species s and photoionization for protons. Loss of He neutrals due to photoionization is also taken into account, but the corresponding source of He<sup>+</sup> ions is not included because we are not tracking He<sup>+</sup> ions in the SW in the present model (as detailed below). The source terms are computed via two Monte Carlo kinetic solvers (Y. G. Malama 1991). The energy transfer due to Coulomb collisions between each ion species with the other species and the effects of turbulence generated by PUIs are also incorporated, as described in F. Fraternale et al. (2023).

For the purpose of this study, we use the helium density and pressure equations to describe He<sup>2+</sup> ions in the SW and He<sup>+</sup> ions in the LISM. We do not include equations for He<sup>+</sup> ions in the SW yet, which is left to a future study. The thermal He<sup>+</sup> ions in the distant SW are mostly produced from alpha particles when they exchange charge with H and He atoms. Electronimpact ionization is the dominant source of He<sup>+</sup> PUIs below 1 au, whereas photoionization is expected to dominate over charge exchange of He atoms with He<sup>2+</sup>, core He<sup>+</sup>, or protons (S. Grzedzielski et al. 2013; K. Scherer et al. 2014; P. Swaczyna et al. 2019b). Ulysses data have also shown that He<sup>+</sup> PUIs are dominant by density as compared with He<sup>2+</sup> PUIs (G. Gloeckler et al. 2004; W. P. Smith et al. 2022). In the future, the presented model will incorporate both He<sup>+</sup> and He<sup>2+</sup>. A valuable aspect of the proposed model is that it allows us to isolate the individual effect of the charge-exchange process  $He^{2+} + He \rightarrow He + He^{2+}$ , which produces He<sup>2+</sup> PUIs. A number of other processes of ionization and recombination will be included in the future versions of our model. Regarding PUIs, in reality, thermal pressure of pickup He<sup>+</sup> ions in the SW is dominant over other helium ions but remains lower than the proton pressure. In the LISM, He<sup>+</sup> ions carry about 40% of mass of all ions, while He<sup>2+</sup> ions are comparatively negligible.

We have fit the helium cross-section data published by C. F. Barnett et al. (1990), obtaining the following expression

for He<sup>2+</sup> ions:

$$\sigma_{\text{cx}}(\text{He} + \text{He}^{2+} \to \text{He}^{2+} + \text{He})$$

$$= \begin{cases} (2.429 - 0.255 \log \mathcal{E})^{1.263} \times 10^{-16} (\text{cm}^2) \text{ for } \mathcal{E} \leqslant 1.54 \text{ keV}, \\ (2.153 - 0.263 \log \mathcal{E})^{1.523} \left[ 1 - \exp\left(-\frac{568}{\mathcal{E}}\right) \right]^{5.32} \times 10^{-16} (\text{cm}^2) & \text{for } 1.54 < \mathcal{E} < 800 \text{ keV}, \end{cases}$$
(A1)

where  $\mathcal{E}$  is the collision energy expressed in keV. The above expressions fit the data with the mean relative error equal to 1.82% and the maximum relative error less than 4% in the energy range  $0.03~{\rm keV} < \mathcal{E} < 800~{\rm keV}$ .

For He<sup>+</sup> ions we use

sharp discontinuity to become smeared over a few cells, depending on the grid resolution and the numerical scheme employed. This smearing is further exacerbated if actual mixing occurs owing to instabilities, turbulence, etc. Typically, a reinitialization of the LS is used to maintain the boundary

$$\sigma_{\text{cx}}(\text{He} + \text{He}^{+} \to \text{He}^{+} + \text{He}) 
= \begin{cases}
(3.24 - 0.288 \log \mathcal{E})^{2} \times 10^{-16} (\text{cm}^{2}) \text{ for } \mathcal{E} \leqslant 2.36 \text{ keV}, \\
(5.07 - 0.707 \log \mathcal{E})^{1.47} \left[ 1 - \exp\left(-\frac{153}{\mathcal{E}}\right) \right]^{0.824} \times 10^{-16} (\text{cm}^{2}) \text{ for } 2.36 < \mathcal{E} < 800 \text{ keV}.
\end{cases}$$
(A2)

The first expression at low energy is the same as was used in our previous studies, while the high-energy expression is added because energetic He atoms are now included in the simulation. In this way, the maximum relative error with respect to the C. F. Barnett et al. (1990) data remains below 1.5% for  $\mathcal{E} < 30~\text{keV}$  and below 3% for higher energies, up to 800 keV. The mean relative error is 0.85% in the whole energy range. Note that the energy threshold used in Equations (A1) and (A2) is chosen to avoid any discontinuity in the cross section.

For (H +H<sup>+</sup>) charge exchange, we used the cross sections from B. G. Lindsay & R. F. Stebbings (2005, hereafter LS05). However, due to the lack of consensus stemming from uncertainties in the available data, particularly at low energies, various other formulae have been proposed (see M. Bzowski & J. Heerikhuisen 2019). In this study we adopt a different approach, e.g., at collision energies  $\mathcal{E} < 3$  keV, we use the new expression proposed by P. Swaczyna et al. (2019a),

$$\sigma_{cx}(H + H^+ \to H^+ + H) = (4.049 - 0.447 \log \mathcal{E})^2$$

$$\times \left[ 1 - \exp\left(-\frac{60.5}{\mathcal{E}}\right) \right]^{4.5} \times 10^{-16} \text{ (cm}^2). \tag{A3}$$

For  $\mathcal{E} \geqslant 3$  keV we keep the LS05 cross-section formula. Note the different fit based on the C. F. Barnett et al. (1990) data proposed by M. Bzowski & J. Heerikhuisen (2019), where the effects of different choices for charge-exchange cross section on global modeling were also discussed.

In addition to the MHD equations, we also solve an LS equation,  $\partial_t \psi(\mathbf{x}, t) + \mathbf{u} \nabla \psi = 0$  (as in S. N. Borovikov et al. 2011), to track the position of the HP. Here the SW and LISM regions are initialized at t=0 with the values  $\psi=-1$  and  $\psi=1$ , the HP being represented by a sharp discontinuity, formally the surface  $\psi=0$ . As far as the LS method is concerned, we clarify that its main purpose is to track an advected surface, so the initialization values are arbitrary. However, as with any other quantity, the LS function is subjected to numerical diffusion, which causes the initially

sharp. However, in the presence of actual mixing/turbulence, reinitialization of the LS may create some issues. In addition, in these situations, the HP can no longer be defined as an ideal tangential discontinuity.

Since the LS smearing has no impact on the solution in kinetic simulations, we decided not to reinitialize the LS and, instead, to use the smearing as a rough indicator of diffusion and mixing, by showing the isocontours  $\psi=\pm 0.98$ , representing approximately the levels where one medium contains 1% in volume of the other medium. However, this approach is extremely approximate. The LS contour lines shown here are for illustration only. They show the numerical solution to the LS equation, which itself describes the convection of tangential discontinuities in the ideal, MHD plasma flow. A detailed study of the mixing requires both a higher resolution, as in S. N. Borovikov & N. V. Pogorelov (2014) and N. V. Pogorelov et al. (2017b), and possibly higher-order differential equations. Detailed description of this phenomenon is beyond the scope of our Letter.

# Appendix B Description of Neutral Atoms: A Method Applicable to Time-dependent Simulations

Our fully 3D, hybrid (MPI+OMP) parallelized kinetic code builds on the previous versions (e.g., J. Heerikhuisen et al. 2006; S. Borovikov et al. 2013). The Boltzmann equations describing the transport of neutral atoms are solved via a Monte Carlo method (Y. G. Malama 1991) using two independent modules, one for H atoms and another for He atoms.

The Monte Carlo method used in MHD-plasma/kinetic-neutrals simulations is an iterative procedure that consists of two alternating stages: the plasma stage and the kinetic stage. The source terms are computed at the kinetic stage, during which the plasma properties and magnetic field are kept constant, while the macroparticles are run for time intervals  $(\tau_{\rm N})$  necessary to gather sufficient statistics. These time intervals are typically very large, for example, we used

 $au_{
m N}\!=\!700\,{
m yr}$  of physical time for solutions presented by F. Fraternale et al. (2023). At the plasma stage, the source terms and positions of neutral particles are frozen, while the MHD solver runs for physical time  $au_{
m pl}$  until the next kinetic stage starts.

It was determined in F. Fraternale et al. (2023) that even for steady-state simulations, especially those with a separate treatment of electrons,  $\tau_{\rm pl}$  needs to be less than  $\sim\!0.3\text{--}0.5$  yr. Larger values may trigger spurious wave-like features in the heliosheath owing to the spatial misalignment between the source terms and the plasma. This is a dangerous situation because it can easily lead to confusion and misinterpretation of the physical phenomena.

If one wishes to resolve scales associated with solar cycle variability (i.e., timescales of a few years and spatial scales of a few au), in nonperiodic solutions, the kinetic-stage parameter  $\tau_{\rm N}$  should be decreased to less than  $\sim\!0.3\,{\rm yr}$  (see V. V. Izmodenov et al. 2005, for an iterative procedure applicable to periodic solution).

From the perspective of plasma solutions, this is important in the presence of inhomogeneities in the properties of neutral atoms that may induce notable changes in the source terms. While this scenario may not always occur, using a small  $\tau_N$  becomes necessary when focusing on the neutral atom distributions.

Furthermore, we impose an additional constraint  $\tau_{\rm N} \equiv \tau_{\rm pl} \equiv \tau$ , which ensures the full self-consistency of the solution by removing any time shifts between individual particles and plasma at the end of each plasma-kinetic sequence.

Reducing the time interval by a factor of about 10<sup>3</sup> while retaining the same statistics is challenging, especially because the finest level of the kinetic grid (used to gather source terms) in our simulations is 1.25 au. Kinetic grids being too coarse would result in unacceptable smearing of the source terms.

We employed an approach based on J. Heerikhuisen et al. (2013; used also by E. J. Zirnstein et al. 2015) consisting of the following procedure:

- 1. For each particle (H and He atoms), simulate many realizations of the same time interval (specifically, we used  $N_{\text{realiz}} = (500 \, \text{yr})/\tau$  and  $\tau = 0.2 \, \text{yr}$ ). During each of these realizations, the initial position and velocity are slightly randomized, and the gathered source terms are eventually averaged. For randomization, we use a Gaussian distribution and establish maximum particle displacements that increase linearly with the heliocentric distance, denoted as  $\delta = \min(0.07|\mathbf{x}_N|, \delta_{\max})$  au, with  $\delta_{\max}$  equal to 50 au in the LISM and 10 au in the SW regions. For each stochastic realization j, we calculate the new particle position  $\mathbf{x}_{N,j} = \mathbf{x}_{N,0} + \delta \left[\frac{2}{\pi} \cos^{-1}(2a-1) 1\right]$ , where  $a \in [-1, 1]$  is a random number drawn from a uniform distribution. After collecting the source terms, only the set of newly born particles resulting from the first realization (not randomized) is retained, and all particles are advanced by a time interval  $\tau$ .
- 2. Tune the parameters of particle splitting and recombination to increase both the actual number of macroparticles per cell (important when deriving neutral atom distributions) and the total number of virtual (split) macroparticles, which determines the number of ionization events per cell (important for accurate computation of source terms) only where this is needed. A macroparticle occupies memory and represents  $N_{\rm split}$  virtual macroparticles with appropriately

weighted mass. In simulation H, we have about  $10^9$  macroparticles for both H and He, but the total number of virtual macroparticles is  $\sim 2 \times 10^9$  for H and  $\sim 8 \times 10^{10}$  for He. Splitting parameters are specific to different atom species, region, and subpopulations. Note that helium requires more particles, due to both the significantly smaller cross sections for charge exchange and the lower He<sup>2+</sup> and He<sup>+</sup> densities in the SW, compared to proton densities (see Figure 2).

The new splitting procedure has two steps. First, similarly to the original version (J. Heerikhuisen et al. 2006), macroparticles are enabled to split at predetermined locations, generating virtual particles, but the actual splitting occurs only during charge exchange. For helium, this may result in fewer macroparticles than needed, so the second step ensures that a new macroparticle is generated even without a charge-exchange event. The initial position randomization is prohibited within 200 au to prevent disruption of the particle's gravitational focusing and the helium cone.

3. Optimize particle distribution across processes to minimize computational time. Particles are distributed based on the number of macroparticles, the number of virtual macroparticles, and the total number of time steps each particle performs within the time interval  $\tau$ .

Our simulation region is a cube of size 1680 au. The timedependent simulation presented in this Letter was run on a Cartesian grid with five levels of refinement, the base grid size being  $\Delta x = \Delta y = \Delta z = 10$  au. The best resolution is  $\sim 0.3$  au cubed, applied everywhere in the SW at heliocentric distances R < 170 au. The resolution of  $\sim 0.625$  au is used elsewhere in the SW regions, including the heliotail, and in the VLISM within 300 au. The source terms from the kinetic modules are collected on parallelepiped-shaped Cartesian kinetic grids, with the finest level size being 1.25 au. The boundaries of the kinetic grids can be identified in panels (e) and (f) of Figure 4. In the Sun-centered coordinates, the finest level of the kinetic grid has the boundaries  $x_{1.25au} \in [-300, 200], y_{1.25au} \in [-150, 150],$  $z_{1.25au} \in [-150, 150]$ , while for the 2.5 au resolution the box boundaries are  $x_{2.5au} \in [-600, 450], y_{2.5au} \in [-350, 350],$  $z_{2.5au} \in [-350, 350]$ . However, they represent a compromise between the computational cost and the goal of maintaining a grid resolution of at least 2.5 au cubed near the whole heliosphere and BS region to prevent excessive smearing of source terms when interpolated onto the plasma grid, which is typically finer. We ran the simulation for about 500 yr of physical time.

#### **ORCID iDs**

Federico Fraternale https://orcid.org/0000-0002-4700-2762 Nikolai V. Pogorelov https://orcid.org/0000-0002-6409-2392

Ratan K. Bera https://orcid.org/0000-0002-4207-3633

#### References

Barnett, C. F., Hunter, H. T., Fitzpatrick, M. I., et al. 1990, Oak Ridge National Laboratory, Report ORNL-6086

Bera, R. K., Fraternale, F., Pogorelov, N. V., et al. 2023, ApJ, 954, 147
Borovikov, S., Heerikhuisen, J., & Pogorelov, N. 2013, in ASP Conf. Ser. 474,
Numerical Modeling of Space Plasma Flows: ASTRONUM-2012, ed.
N. V. Pogorelov, E. Audit, & G. P. Zank (San Francisco, CA: ASP), 219
Borovikov, S. N., & Pogorelov, N. V. 2014, ApJL, 783, L16

```
Borovikov, S. N., Pogorelov, N. V., Burlaga, L. F., & Richardson, J. D. 2011,
   ApJL, 728, L21
Bzowski, M., Czechowski, A., Frisch, P. C., et al. 2019, ApJ, 882, 60
Bzowski, M., & Heerikhuisen, J. 2019, ApJ, 888, 24
DeStefano, A. M., & Heerikhuisen, J. 2020, PhPl, 27, 032901
Fraternale, F., & Pogorelov, N. V. 2021, ApJ, 906, 75
Fraternale, F., Pogorelov, N. V., & Bera, R. K. 2023, ApJ, 946, 97
Fraternale, F., Pogorelov, N. V., & Bera, R. K. 2024, JPCS, 2742, 012011
Fraternale, F., Pogorelov, N. V., & Heerikhuisen, J. 2021, ApJL, 921, L24
Gloeckler, G., Möbius, E., Geiss, J., et al. 2004, A&A, 426, 845
Grzedzielski, S., Swaczyna, P., & Bzowski, M. 2013, A&A, 549, A76
Gurnett, D. A., Kurth, W. S., Burlaga, L. F., et al. 2021, ApJ, 921, 62
Heerikhuisen, J., Florinski, V., & Zank, G. P. 2006, JGRA, 111, A06110
Heerikhuisen, J., Gamayunov, K. V., Zirnstein, E. J., & Pogorelov, N. V. 2016,
   ApJ, 831, 137
Heerikhuisen, J., Pogorelov, N. V., & Zank, G. P. 2013, in ASP Conf. Ser. 474,
   Numerical Modeling of Space Plasma Flows: ASTRONUM-2012, ed.
  N. V. Pogorelov, E. Audit, & G. P. Zank (San Francisco, CA: ASP), 195
Heerikhuisen, J., Pogorelov, N. V., Zank, G. P., et al. 2010, ApJL, 708, L126
Izmodenov, V. V., & Alexashov, D. B. 2020, A&A, 633, L12
Izmodenov, V. V., Malama, Y. G., & Ruderman, M. S. 2005, A&A, 429, 1069
Kim, T., Kryukov, I., Pogorelov, N., Elliott, H., & Zank, G. P. 2018, esoar,
   553, essoar.b60497724eca58de
Kim, T. K., Pogorelov, N. V., & Burlaga, L. F. 2017, ApJL, 843, L32
Kornbleuth, M., Opher, M., Dayeh, M. A., et al. 2024, ApJL, 967, L12
Kurth, W. S. 2024, ApJL, 963, L6
Lallement, R., Quemerais, E., Bertaux, J. L., et al. 2005, Sci, 307, 1447
Lindsay, B. G., & Stebbings, R. F. 2005, JGRA, 110, A12213
Malama, Y. G. 1991, Ap&SS, 176, 21
McComas, D. J., Allegrini, F., Bochsler, P., et al. 2009, Sci, 326, 959
McComas, D. J., Bzowski, M., Fuselier, S. A., et al. 2015, ApJS, 220, 22
McComas, D. J., Christian, E. R., Schwadron, N. A., et al. 2018, SSRv,
   214, 116
```

```
McComas, D. J., Shrestha, B. L., Swaczyna, P., et al. 2022, ApJS, 934, 147
Mostafavi, P., Allen, R. C., McManus, M. D., et al. 2022, ApJL, 926, L38
Neugebauer, M., Goldstein, B. E., Smith, E. J., & Feldman, W. C. 1996,
   JGRA, 101, 17047
Ocker, S., Cordes, J., Chatterjee, S., et al. 2021, NatAs, 5, 761
Pogorelov, N. V., Borovikov, S. N., Heerikhuisen, J., & Zhang, M. 2015,
   ApJL, 812, L6
Pogorelov, N. V., Borovikov, S. N., Zank, G. P., & Ogino, T. 2009, ApJ,
Pogorelov, N. V., Fichtner, H., Czechowski, A., et al. 2017a, SSRv, 212, 193
Pogorelov, N. V., Fraternale, F., Kim, T. K., Burlaga, L. F., & Gurnett, D. A.
  2021, ApJ, 917, L20
Pogorelov, N. V., Heerikhuisen, J., Roytershteyn, V., et al. 2017b, ApJ,
Powell, E., Opher, M., Kornbleuth, M. Z., et al. 2024, ApJ, 961, 235
Reisenfeld, D. B., Bzowski, M., Funsten, H. O., et al. 2021, ApJS, 254, 40
Richardson, J. D., Belcher, J. W., Garcia-Galindo, P., & Burlaga, L. F. 2019,
    VatAs, 3, 1019
Scherer, K., Fichtner, H., Fahr, H.-J., Bzowski, M., & Ferreira, S. E. S. 2014,
   A&A, 563, A69
Slavin, J. D., & Frisch, P. C. 2008, A&A, 491, 53
Smith, W. P., Renfroe, K., Pogorelov, N. V., et al. 2022, ApJ, 933, 124
Swaczyna, P., Bzowski, M., Dialynas, K., et al. 2024, ApJL, 969, L20
Swaczyna, P., Bzowski, M., Heerikhuisen, J., et al. 2023, ApJ, 953, 107
Swaczyna, P., McComas, D. J., & Schwadron, N. A. 2019a, ApJ, 871, 254
Swaczyna, P., McComas, D. J., & Zirnstein, E. J. 2019b, ApJ, 875, 36
Swaczyna, P., McComas, D. J., Zirnstein, E. J., et al. 2020, ApJ, 903, 48
Wood, B. E., Müller, H.-R., & Möbius, E. 2019, ApJ, 881, 55
Zank, G. P. 2015, ARA&A, 53, 449
Zank, G. P., Heerikhuisen, J., Pogorelov, N. V., et al. 2013, ApJ, 763, 20
Zirnstein, E. J., Heerikhuisen, J., Funsten, H. O., et al. 2016, ApJL, 818, L18
Zirnstein, E. J., Heerikhuisen, J., Pogorelov, N. V., McComas, D. J., &
  Dayeh, M. A. 2015, ApJ, 804, 5
```